Title

Zonal flow screening in negative triangularity tokamaks

Permalink

Journal

ISSN

Authors

Singh, Rameswar
Diamond, PH

Publication Date

DOI

Peer reviewed

Zonal flow screening in negative triangularity tokamaks

Rameswar Singh

E-mail: `rsingh@ucsd.edu`

P H Diamond

CASS, University of California San Diego, 9500 Gilman Dr, La Jolla, CA 92093,

United States of America

Abstract. This paper presents a comparative study of zonal flow screening in positive and negative triangularity tokamaks. Neoclassical screening sets the strength of zonal flow shear for fixed drive and damping. Orbit calculations show that the radial excursions of trapped particles are reduced in negative triangularity tokamaks, as compared to positive triangularity. Yet surprisingly, the neoclassical dielctric susceptibility actually increases with decreasing triangularity, such that the susceptibility is higher for negative triangularity than for positive triangularity. This is because the reduction in neoclassical polarization by shrinking the banana width is offset by the increase in neoclassical polarization by the enhancement of trapped fraction for negative triangularity. As a result, the zonal flow screening length is actually enhanced for negative triangularity, as compared to positive triangularity. Hence, the zonal flow residual is smaller for negative triangularity than for positive triangularity. Results from gyrokinetic simulations support the analytic calculations.

1. Introduction

Negative triangularity (NT) discharges have achieved high confinement (H) mode-like pressure and energy confinement times for low confinement (L) mode [1–5] edge conditions. However, unlike conventional H mode [6, 7] for positive triangularity, negative triangularity L mode discharges exhibit no undesirable features like edge localized modes (ELMs) or bursty MHD, because no pedestal forms in L mode. While ELMs in positive triangularity H mode can be suppressed by externally applied RMPs [8] etc., NT L mode is an attractive operation regime that is *naturally* free of ELMs. Also, NT discharges manifest very weak degradation of confinement with power [1], along with broader scrape off layer (SOL) heat flux widths, reduced fluctuation levels [1–4] and reduced plasma wall interaction [9]. NT plasmas show strong resilience and tend to stay in L mode well beyond the L-H transition power threshold for matched positive triangularity plasmas. These attractive features make NT L mode a potential candidate for a fusion reactor [10, 11]. Hence, a clear understanding of the physics of confinement improvement in negative triangularity is desirable. This begs for a study of the mechanism of turbulence saturation in negative triangularity shapes.

The turbulence in tokamaks is usually some sort of drift wave turbulence, excited by instabilities linked to the equilibrium density, temperature gradients and magnetic field curvature. Turbulence causes transport and thus limits the confinement time. There have been gyrokinetic simulation studies showing reduction of turbulence and transport in the core of NT configuration [3, 4, 12–15]. All these simulations attribute a linear stabilization of trapped electron mode (TEM) or ion temperature gradient (ITG) mode to the observed reduction of core turbulence and transport in NT. Little attention has been paid to the actual mechanisms of turbulence saturation in NT. A simple story of linear mode growth rate reduction cannot explain the turbulence saturation at lower

levels in NT. The linear physics propagates into the quasilinear theory. Hence, we expect simple quasilinear theory to be also inadequate for explaining the confinement improvement in NT.

Drift wave turbulence also supports zonal flows, which are a poloidally symmetric and radially sheared ExB flows [16]. Zonal flows are nonlinearly excited by turbulent negative (zonal) eddy viscosity effect [17] and the polarization beat noise [16, 18]. Negative eddy viscosity results from the coherent mode couplings and manifest as inverse cascade of kinetic energy. The beat noise results from the incoherent mode couplings. The interaction of zonal noise and modulations has a significant effect on feedback processes [18]. Radial shear of the zonal flow breaks up turbulent eddies, thus reducing the turbulence coherence length [19]. As a result, transport is reduced upon excitation of zonal flows. This feedback effect on drift wave turbulence appears as diffusion of turbulence energy (in the radial wave number spectral domain) induced by the zonal flow shear spectrum. The spectral diffusion of turbulence is from low to high radial wave numbers, where the turbulence intensity is lower. The strength of the feedback effect depends on the magnitude of the zonal flow shear. So zonal flow excitation is a mechanism of turbulence saturation.

This motivates a comparative study of zonal flows in positive and negative triangularity tokamaks. The spectral evolution of zonal intensity‡ shows that the zonal flow shear strength is determined by the ion dielectric susceptibility χ_k, for fixed drive. Dielectric susceptibility here means susceptibility to dielectric polarization. Departure of

---

‡ Zonal intensity $\left\langle \left\langle |\phi_k|^2 \right\rangle \right\rangle$ evolves as:

$$\frac{\partial}{\partial t} \chi_k \left\langle \left\langle |\phi_k|^2 \right\rangle \right\rangle = \Re \sum_{\vec{k}=\vec{p}+\vec{q}} \hat{z} \cdot \vec{p} \times \vec{q} \left(q^2 - p^2 \right) \left\langle \left\langle \phi_k^\star \phi_p \phi_q \right\rangle \right\rangle .$$

Here $\vec{k} = k_r \hat{r}$ refers to the zonal mode wave vector. $\vec{p}$ and $\vec{q}$ refers to the turbulent modes wave vectors. $\langle\langle \cdots \rangle\rangle$ represents ensemble average. Total ion dielectric susceptibility χ_k is sum of classical and neoclassical dielectric susceptibilities i.e., $\chi_k = \chi_{k,cl} + \chi_{k,neo}$.

particle from the magnetic flux surface leads to polarization. Two types of polarization are possible - classical polarization and neoclassical polarization. Classical polarization results from the departure of particle from the magnetic flux surface due to gyro-motion. Neoclassical polarization results from the departure of the guiding center from the flux surface due to magnetic drift. The total dielectric susceptibility χ_k is simply the sum of classical and neoclassical dielectric susceptibilities i.e, $\chi_k = \chi_{k,cl} + \chi_{k,neo}$. It turns out that $\chi_{k,cl} \sim k_r^2 \rho_i^2$ and $\chi_{k,neo} \sim k_r^2 \rho_\theta^2$ in the long wave length limit ($k_r \rho_\theta \ll 1$), where ρ_i is the ion thermal gyro-radius, ρ_θ is the poloidal gyro-radius and k_r is radial wave number of the zonal mode. Usually $\rho_\theta \gg \rho_i$ hence, $\chi_{k,neo} \gg \chi_{k,cl}$. As a result the zonal flow screening length (which is a proxy for the zonal flow scale length), given by $\sqrt{\chi_k / k_r^2}$, is primarily determined by the neoclassical dielectric susceptibility $\chi_{k,neo}$. Smaller (bigger) screening length implies stronger (weaker) zonal flows. Thus, it is natural to study the effect of triangularity on the ion susceptibility. Heuristically, trapped particle radial excursion is related to neoclassical polarization, in that smaller (bigger) banana width implies weaker (stronger) polarization. Orbit calculations show that the radial banana width in NT is smaller than for positive triangularity. Thus, one expects smaller $\chi_{k,neo}$ → smaller neoclassical screening length → stronger zonal flow shear in NT. Surprisingly, calculations actually show *larger $\chi_{k,neo}$ → larger screening length → smaller zonal flow shear in NT.*

The rest of the paper is organized as follows. The variations of classical, and neoclassical dielectric susceptibilities and zonal flow screening lengths with triangularity are discussed in detail in Section(2). It is shown that the neoclassical dielectric susceptibility is higher (and hence the level of zonal flow residual is lower) in NT than for positive triangularity, despite the reduction of banana widths in NT. GENE simulations, which support the analytic results, are also presented. This counter - intuitive result

can be reconciled by considering the triangularity effects on particle orbits. This is discussed in detail in Section(3), where it is argued that polarization reduction due to banana width reduction is offset by the polarization increase due to the trapped fraction increase. Finally, Section(4) gives discussion and conclusions. The mathematical details of the dielectric susceptibility calculations are presented in Appendix A and Appendix B.

2. Zonal flow residual: Analytic calculations and comparison with simulations

Following the Hinton-Rosenbluth prescription [20], the residual zonal flow level can be obtained as

$$\phi_k(\infty) = \phi_k(0)\frac{\chi_{k,cl}}{\chi_{k,cl} + \chi_{k,neo}}, \tag{1}$$

where $\chi_{k,cl}$ is classical dielectric susceptibility and $\chi_{k,neo}$ is neoclassical dielectric susceptibility. Here, classical dielectric susceptibility means the susceptibility to classical polarization and neoclassical dielectric susceptibility means the susceptibility to neoclassical polarization. The classical dielectric susceptibility in the long wavelength $(k_r\rho_\theta \ll 1)$ and collisionless limit is given by

$$\chi_{k,cl} = \left\langle k_r^2 \rho_i^2 \right\rangle = \frac{m_i T_i}{e^2}\left\langle k_r^2/B^2 \right\rangle. \tag{2}$$

Here, the radial wave vector is $\vec{k}_r = \vec{\nabla}S$, where S is the phase of the perturbed quantities and is a function of flux coordinate ψ. The neoclassical dielectric susceptibility in the long wavelength $(k_r\rho_\theta \ll 1)$ and the collisionless limit are given by

$$\chi_{k,neo} = \frac{1}{n_0}\left\langle \int d^3v F_M Q \left[Q - \overline{Q}\right] \right\rangle. \tag{3}$$

Here, $Q = \frac{m_i I S' v_\parallel}{eB} = k_r \rho_\theta$, $S' = \frac{\partial S}{\partial \psi}$ and F_M is local Maxwellian distribution. Q represents the effect of the deviation of guiding center from the bounce or transit center The angular braces represents flux surface averages: $\langle A \rangle = \frac{\int d\theta J A}{\int d\theta J}$ is flux surface average, where $J = \frac{1}{|\vec{\nabla}\zeta \times \vec{\nabla}\psi \cdot \vec{\nabla}\theta|} = \frac{1}{|\vec{B} \cdot \vec{\nabla}\theta|}$ is the Jacobian. Over lines represent bounce average: $\overline{A} = \frac{\int d\theta J \frac{B}{v_\parallel} A}{\int d\theta J \frac{B}{v_\parallel}}$ is bounce average of A. The classical susceptibility /polarization is due to the departure of the particle from the flux surface due to the gyro motion. The neoclassical polarization is due to the departure of the guiding center from the flux surfaces due to magnetic drifts. To calculate $\langle A \rangle$ and $\overline{A}$ the shape of the flux surfaces are required. This is described in the following sub-section, and the subsequent sub-sections describe the calculations of dielectric susceptibilities.

2.1. Magnetic Equilibrium

To specify the flux surface shape, we use the local parametrized model for up-down symmetric D shaped plasmas developed by Miller et *al* [21]

$$R = R_0(r) + r\cos(y) = R_0 h \tag{4}$$

$$Z = \kappa(r) r \sin\theta \tag{5}$$

Here, $h = 1 + \epsilon\cos(y)$ is the radial scale factor, $\epsilon = \frac{r}{R_0}$ is the running inverse aspect ratio, $y = \theta + x\sin\theta$, and $x = \sin^{-1}\delta(r)$. Here δ is triangularity and κ is ellipticity or elongation. Note that r, the minor radius, is a flux function i.e., $r = r(\psi)$. The primary advantage of this model compared with a full numerical equilibrium is that the parameters can be individually varied. This allows for systematic studies of the effects of each parameter upon stability and transport for shaped flux surfaces. Here, we focus on the effect of triangularity (δ)(see figure(1)) on the zonal flow screening. The magnetic
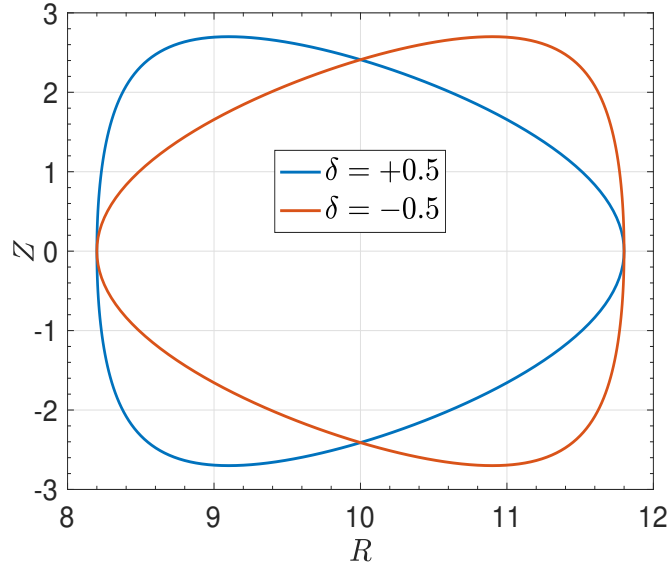
Figure 1. Flux surface shapes for positive and negative triangularities.

field is defined in flux coordinates (ψ, θ, ζ) as:

$$\vec{B} = I\vec{\nabla}\zeta + \vec{\nabla}\zeta \times \vec{\nabla}\psi. \tag{6}$$

The poloidal magnetic field is given by

$$B_p = \left|\vec{\nabla}\zeta \times \vec{\nabla}\psi\right| = \frac{\partial_r\psi}{R}\left|\vec{\nabla}r\right| = \frac{\partial_r\psi}{\mathcal{J}}\sqrt{g_{\theta\theta}}, \tag{7}$$

where $\mathcal{J}$ is Jacobian $\mathcal{J} = \frac{\partial\vec{r}}{\partial r}\cdot\frac{\partial\vec{r}}{\partial\theta}\times\frac{\partial\vec{r}}{\partial\zeta} = \frac{1}{\vec{\nabla}r\cdot\vec{\nabla}\theta\times\vec{\nabla}\zeta} = J\partial_r\psi$ and $\vec{r} = R\cos\zeta\,\hat{x} + R\sin\zeta\,\hat{y} + Z\hat{z}$.

The last step in the above equation is obtained using $\left|\vec{\nabla}r\right| = \frac{R}{\mathcal{J}}\sqrt{g_{\theta\theta}}$, which follows from

the conjugate relation $\vec{\nabla}r = \frac{1}{\mathcal{J}}\frac{\partial\vec{r}}{\partial\theta}\times\frac{\partial\vec{r}}{\partial\zeta}$. Note that complete determination of B_p requires

explicit expressions of the poloidal flux gradient $\partial_r\psi$, the Jacobian $\mathcal{J}$ and the metric

tensor element $g_{\theta\theta}$. These are calculated as follows. The Jacobian $\mathcal{J}$ can be calculated

explicitly as

$$\mathcal{J} = R\kappa r\left[R'_0\cos(\theta) + \cos(x\sin\theta) + \sin(y)\sin\theta\left\{S_\kappa - S_\delta\cos\theta + (1 + S_\kappa)x\cos\theta\right\}\right], \tag{8}$$

where $R'_0 = \frac{\partial R_0}{\partial r}$ is Shafranov shift, $S_\kappa = \frac{r}{\kappa}\frac{\partial\kappa}{\partial r}$ is ellipticity gradient, and $S_\delta = \frac{r\frac{\partial\delta}{\partial r}}{\sqrt{1-\delta^2}}$ is

triangularity gradient. Here we assume R'_0, S_κ and S_δ are independent parameters. The

metric tensor element $g_{\theta\theta}$ can be obtained as:

$$g_{\theta\theta} = \frac{\partial \vec{r}}{\partial \theta} \cdot \frac{\partial \vec{r}}{\partial \theta} = r^2 \sin^2 y \left[1 + x \cos \theta\right]^2 + \kappa^2 r^2 \cos^2 \theta. \tag{9}$$

The poloidal flux gradient $\partial_r \psi$ can be obtained from the definition of the safety factor $q(\psi) = \oint d\theta \frac{\vec{B} \cdot \vec{\nabla}\zeta}{\vec{B} \cdot \vec{\nabla}\theta} / \oint d\theta$ as:

$$\partial_r \psi = \frac{I(\psi)}{2\pi q(\psi)} \oint d\theta \frac{\mathcal{J}}{R^2}. \tag{10}$$

Hence, the poloidal magnetic field becomes

$$B_p = \frac{\sqrt{g_{\theta\theta}}}{\mathcal{J}} \frac{I(\psi)}{2\pi q(\psi)} \oint d\theta \frac{\mathcal{J}}{R^2}. \tag{11}$$

For small inverse aspect ratio ($\epsilon \ll 1$), the integral can be written in terms of the power series yielding the flux gradient as

$$\partial_r \psi = \frac{I(\psi)\kappa}{2\pi q(\psi)} \epsilon \sum_{i=0}^{\infty} (-1)^i \epsilon^i F_i. \tag{12}$$

Hence, the poloidal magnetic field for $\epsilon \ll 1$ becomes

$$B_p = \frac{\sqrt{g_{\theta\theta}}}{\mathcal{J}} \frac{I(\psi)\kappa}{2\pi q(\psi)} \epsilon \sum_{i=0}^{\infty} (-1)^i \epsilon^i F_i. \tag{13}$$

The first few terms of the set $\{F_i\}$ in the above equation(12) are:

$$
\left\{
\begin{aligned}
F_0 &= 2\pi J_0(x) + S_\kappa \pi \left(J_0(x) - J_2(x)\right) + \left\{(1 + S_\kappa)\, x - S_\delta\right\} \tfrac{\pi}{2} \left(J_1(x) + J_3(x)\right) \\[4pt]
F_1 &= R_0' \pi \left(J_2(-x) + J_0(-x)\right) + \pi J_1(-2x) + S_\kappa \tfrac{\pi}{2} \left(J_1(-2x) - J_3(2x)\right) \\[4pt]
&\quad + \left\{(1 + S_\kappa)\, x - S_\delta\right\} \tfrac{\pi}{4} \left(J_0(2x) - J_4(2x)\right) \\[4pt]
F_2 &= R_0' \tfrac{\pi}{2} \left(J_3(-2x) + J_1(-2x)\right) + \tfrac{\pi}{2} \left(J_2(-3x) + J_2(-x) + 2J_0(x)\right) \\[4pt]
&\quad + S_\kappa \tfrac{\pi}{4} \left(J_2(-3x) - J_4(-3x)\right) \\[4pt]
&\quad + \left\{(1 + S_\kappa)\, x - S_\delta\right\} \tfrac{\pi}{8} \left(J_1(-3x) + J_1(x) - J_5(-3x) - J_3(-x)\right) \\[4pt]
F_3 &= R_0' \tfrac{\pi}{4} \left(J_4(-3x) + J_2(-3x) + 3J_2(-x) + 3J_0(x)\right) \\[4pt]
&\quad + \tfrac{\pi}{4} \left(J_3(-4x) + J_3(-2x) + 3J_1(-2x)\right) \\[4pt]
&\quad + S_\kappa \tfrac{\pi}{8} \left(J_3(-4x) - J_5(-4x) + 2J_1(-2x) - 2J_3(-2x)\right) \\[4pt]
&\quad + \left\{(1 + S_\kappa)\, x - S_\delta\right\} \tfrac{\pi}{16} \left(J_2(-4x) - J_6(-4x) + J_0(2x) - J_4(-2x)\right) \\[4pt]
\cdots \quad \cdots & \qquad\qquad\qquad\qquad \cdots
\end{aligned}
\right\}
\tag{14}
$$

Here $J_n(mx)$ is the nth order Bessel functions of 1st kind defined by $J_n(mx) = \frac{1}{2\pi} \oint \cos(n\theta - mx\sin\theta)$. Notice that $J_n(x) = J_n(-x)$ for $n = 0, 2, 4, \cdots etc.$, and $J_n(x) = -J_n(-x)$ for $n = 1, 3, 5, \cdots, etc.$ As a result the terms $\{F_i\}$ are asymmetric with respect to the sign of triangularity δ. This makes the flux gradient $\partial_r \psi$ and the poloidal magnetic field B_p asymmetric with respect to a change in the sign of triangularity δ. Notice that terms $\{F_i\}$ have parametric dependence on triangularity δ, triangularity gradient S_δ and elongation gradient S_κ, but are independent of elongation κ. The poloidal magnetic field B_p depends on κ only through the metric tensor element $g_{\theta\theta}$. The In the following, we calculate the classical dielectric susceptibility, neoclassical dielectric susceptibility and the zonal flow residual and discuss their variations with triangularity. Effects of ellipticity/ elongation κ are discussed in the (Appendix C).

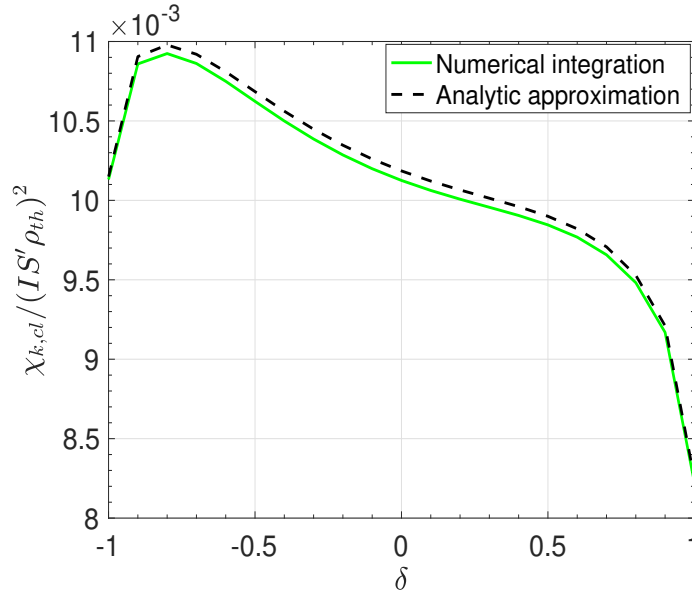*2.2. Variation of classical dielectric susceptibility $\chi_{k,cl}$ with triangularity δ*

As shown in Appendix A, the classical dielectric susceptibility for small inverse aspect ratio ($\epsilon \ll 1$) can be obtained as:

$$\chi_{k,cl} = (S'I(\psi)\rho_{th})^2 \left(\frac{1}{2\pi q(\psi)}\right)^2 \frac{\epsilon^2 \left[\sum_{i=0}^{\infty}(-1)^i\epsilon^i F_i\right]^2 f}{[F_0 + \epsilon F_1]}, \tag{15}$$

where the set $\{F_i\}$ is given by equation(14) and f is given by equation(A.3). For the concentric circular equilibrium, the equation(15) takes the familiar form:

$$\chi_{k,cl}^{circular} = \frac{m_iT_i}{e^2}\left\langle k_r^2/B^2\right\rangle_{circular} = (S'I(\psi)\rho_{th})^2\left[\frac{\epsilon^2}{q^2} + h.o.t\right]. \tag{16}$$

Figure(2) shows plot of $\chi_{k,cl}$ as a function of δ. Clearly, the classical dielectric susceptibility increases with decreasing δ such that classical dielectric susceptibility is higher for $\delta < 0$ than for $\delta > 0$ i.e., $\chi_{k,cl}(\delta^-) > \chi_{k,cl}(\delta^+)$.

Figure 2. Variation of classical dielectric susceptibility $\chi_{k,cl}$ with triangularity δ. $\chi_{k,cl}$ increases with decreasing δ such that $\chi_{k,cl}(\delta^-) > \chi_{k,cl}(\delta^+)$. Analytic approximation correspond to equation(15). Numerical integration correspond to exact numerical calculation of $\left\langle k_r^2/B^2\right\rangle$. Parameters: $\frac{\partial R_0}{\partial r} = -0.4$, $S_\delta = 0.4$, $\kappa = 1.5$, $S_\kappa = 1$, $\epsilon = 0.18$, $q = 3$.

2.3. Variation of neoclassical dielectric susceptibility $\chi_{k,neo}$ with triangularity

Here we discuss the variation of neoclassical dielectric susceptibility with triangularity. The details of the derivation of $\chi_{k,neo}$ are shown in Appendix B. After tedious but straight forward algebra, the neoclassical dielectric susceptibility can be obtained as:

$$\chi_{k,neo} = (IS'\rho_{th})^2 \left[\frac{F_0 + 3\epsilon F_1 + 3\epsilon^2 F_2 + \epsilon^3 F_3}{F_0 + \epsilon F_1} - \left(1 + \epsilon\frac{F_1}{F_0}\right) \left(1 + \epsilon\frac{F_1}{F_0} + \sum_{i=1}^{\infty} \epsilon^{1+i/2} A_{1+i/2}\right) \right],$$

(17)

where the set $\{F_i\}$ is given by equation(14) and the first few terms of the $\{A_{1+i/2}\}$ are given by

$$\begin{cases} A_{3/2} &= -1 - \frac{3}{2}\frac{F_1}{F_0} - \frac{9}{8}\frac{F_2}{F_0} + \frac{5}{16}\frac{F_3}{F_0} \\ A_2 &= 2\frac{F_2}{F_0} \\ A_{5/2} &= \frac{1}{2}\frac{F_1}{F_0} - \frac{3}{4}\frac{F_2}{F_0} - \frac{9}{16}\frac{F_3}{F_0} \\ A_3 &= 0 \\ A_{7/2} &= -\frac{1}{8}\frac{F_2}{F_0} + \frac{3}{16}\frac{F_3}{F_0} \\ \dots \quad \dots & \quad \dots \end{cases}.$$

(18)

For the concentric circular equilibrium, the above equation takes the familiar form

$$\chi_{k,neo}^{circular} = (IS'\rho_{th})^2 \left[1.563\epsilon^{3/2} + \frac{1}{2}\epsilon^2 + \frac{3}{8}\epsilon^{5/2} + \frac{1}{16}\epsilon^{7/2} + ... \right].$$

(19)

The variation of χ_{neo} with δ is shown in figure(3). It is clear that χ_{neo} is higher for $\delta < 0$ than that for $\delta > 0$.
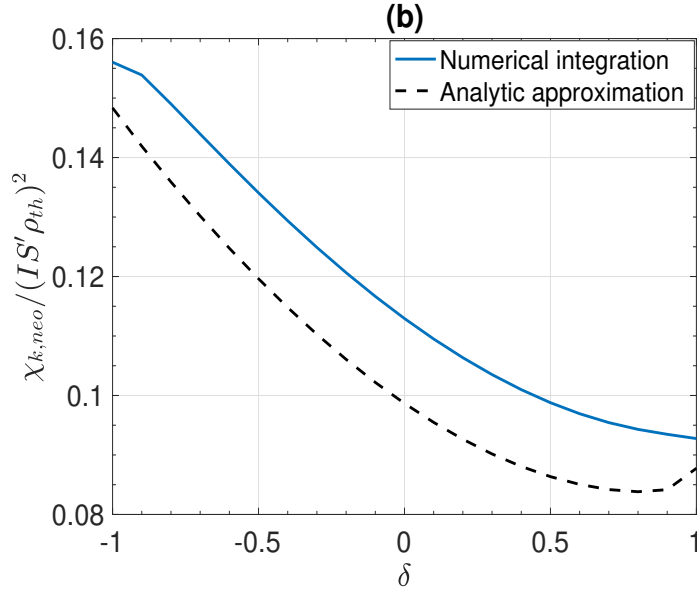
Figure 3. Neoclassical dielectric susceptibility is higher for $\delta < 0$ than that for $\delta > 0$. The solid curve is from numerical integration. Black dashed curve is from the analytic approximation equation(17). The solid curve corresponds to the result obtained using the numerical integration of equations(B.1) and (B.5) Parameters: $\frac{\partial R_0}{\partial r} = -0.4$, $S_\delta = 0.4$, $\kappa = 1.5$, $S_\kappa = 1$, $\epsilon = 0.18$, $q = 3$.

2.4. Variation of zonal flow residual and the zonal flow screening length with triangularity

Finally, using equations(15) and (17), the expression for the zonal flow residual becomes

$$\phi_k(\infty) = \frac{\phi_k(0)}{1 + \frac{q^2}{\epsilon^2}\Theta},\tag{20}$$

where the shaping function is given by

$$\Theta = \left[\frac{F_0 + 3\epsilon F_1 + 3\epsilon^2 F_2 + \epsilon^3 F_3}{F_0 + \epsilon F_1} - \left(1 + \epsilon\frac{F_1}{F_0}\right)\left(1 + \epsilon\frac{F_1}{F_0} + \sum_{i=1}^{\infty}\epsilon^{1+i/2}A_{1+i/2}\right) \right]$$
$$\times \frac{(2\pi)^2\left[F_0 + \epsilon F_1\right]}{\left[\sum_{i=0}^{\infty}(-1)^i\epsilon^i F_i\right]^2 f}.\tag{21}$$

For the concentric circular equilibrium, the shaping factor becomes $\Theta \approx 1.6\epsilon^{3/2}$ to the lowest order in ϵ. Figure(4) compares plots of the residual zonal flow level vs triangularity obtained from the small inverse aspect ratio analytic calculation, numerical integration of the integrals and linear gyrokinetic GENE simulations [22, 23]. GENE

simulations were set-up for a linear initial value calculation of zonal potential relaxation, a typical Hinton-Rosenbluth test. A flux surface averaged potential is initialized and its evolution is tracked in time. The simulation is run until time $t = 100R/c_s$. The time asymptotic undamped part of potential, left after the geodesic acoustic mode oscillations have damped, is called the residual potential and the associated $E \times B$ flow is called the residual zonal flow. In practice, the residual level here is obtained by time averaging the flux surface averaged potential in the interval $t = [10, \quad 100]R/c_s$. This time interval has been found to be sufficient for the convergence of the running average of the zonal potential. All simulations were done for the zonal wave number $k_r \rho_{i,th} = 0.05$, which is representative of zonal flows at length scales relevant to ITG saturation. The figure clearly shows that *the level of the residual zonal flow decreases with decreasing triangularity, such that the residual level is lower for negative triangularity than that for positive triangularity. This means that the zonal flow screening length l_z, defined by $l_z = \rho_s \sqrt{1 + \frac{q^2}{\epsilon^2}\Theta}$, increases with decreasing triangularity such that $l_z(\delta^-) > l_z(\delta^+)$.* Notice that $\chi_{k,neo} \gg \chi_{k,cl}$, which means the reduction of zonal flow residual for negative triangularity (as compared to matched positive triangularity) is due to the increase in $\chi_{k,neo}$ for negative triangularity. Then, one naturally wonders what are the relative contributions of passing and trapped particle in enhancing the $\chi_{k,neo}$ in negative triangularity? This begs for a calculation of the pitch angle spectra $\chi_{k,neo}(\lambda)$ of the neoclassical susceptibility. Finally, it is also possible to study elongation κ dependence of the zonal flow residual. This is presented in the (Appendix C).
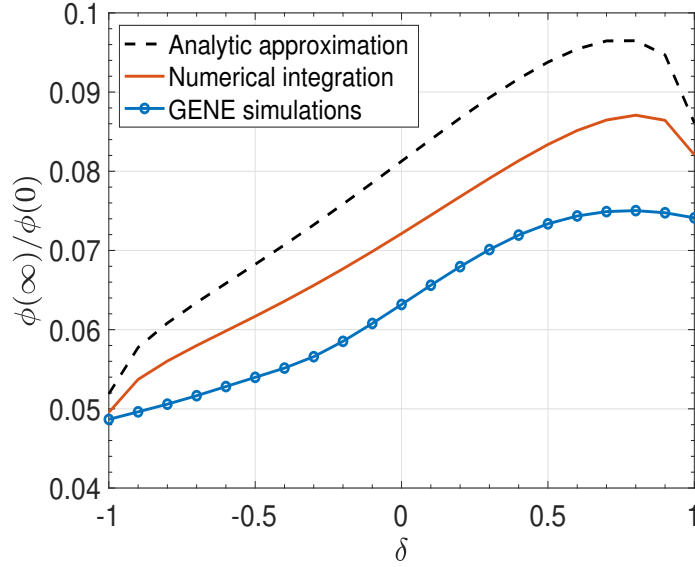
Figure 4. Residual zonal flow level is lower at negative δ than at positive δ. Parameters: $\frac{\partial R_0}{\partial r} = -0.4$, $S_\delta = 0.4$, $\kappa = 1.5$, $S_\kappa = 1$, $\epsilon = 0.18$, $q = 3$. The analytic approximation corresponds to the small inverse aspect ratio calculation given by equation(20).

2.5. Variation of pitch-angle spectrum of neoclassical dielectric susceptibility $\chi_{k,neo}$ with triangularity

It is useful to extract the contributions of trapped and passing particles in setting up the level of the neoclassical dielectric susceptibility. The neoclassical dielectric susceptibility is given by

$$
\begin{aligned}
\chi_{k,neo} &= \frac{m_i(IS')^2}{n_0 e^2} \left\langle \int d^3v F_M \frac{v_\parallel}{B} \left[\frac{v_\parallel}{B} - \overline{\left(\frac{v_\parallel}{B} \right)} \right] \right\rangle \\
&= (IS'\rho_{th})^2 \frac{1}{n_0 v_{th}^2} \left\langle \int d^3v F_M v_\parallel h \left[v_\parallel h - \overline{v_\parallel h} \right] \right\rangle \\
&= (IS'\rho_{th})^2 \frac{3}{2} \left[\left\{ \int_0^{1-\epsilon} d\lambda P_1(\lambda) + \int_{1-\epsilon}^{1+\epsilon} d\lambda P_2(\lambda) \right\} - \int_0^{1-\epsilon} d\lambda P_3(\lambda) \right] \\
&= \int_0^{1+\epsilon} d\lambda \chi_{k,neo}(\lambda),
\end{aligned}
$$

where $P_1(\lambda) = \frac{\oint d\theta \mathcal{J} h\xi}{\oint d\theta \mathcal{J}}$, $P_2(\lambda) = \frac{\int_{-\theta_b}^{+\theta_b} d\theta \mathcal{J} h\xi}{\oint d\theta \mathcal{J}}$ and $P_3(\lambda) = \frac{\oint d\theta \mathcal{J}}{\oint d\theta \mathcal{J}/h\xi}$. The pitch angle spectra of neoclassical dielectric susceptibility is shown in figure(5). Notice that the distribution peaks at the trapped - passing boundary. The passing particle contribution to the total

neoclassical susceptibility is much smaller than the trapped particles contribution. Also, triangularity variations dominantly affect the trapped part of the spectrum. The passing part of the pitch angle spectrum is very weakly affected by the variations in triangularity. The trapped part of the spectrum is elevated upon lowering the triangularity, so that that the neoclassical dielectric susceptibility is higher for $\delta < 0$ than that for $\delta > 0$. These results make one speculate that the radial excursion of trapped particles must be bigger in negative triangularity than for positive triangularity. However, calculations show that *the actual radial excursions are smaller in negative triangularity than that in positive triangularity.* Thus, how can we reconcile the trend in δ of $\chi_{k,neo}$ with the effects of δ on particle orbits? This begs for a detailed comparative study of particle orbits in positive and negative triangularity. This study is presented in the following section.
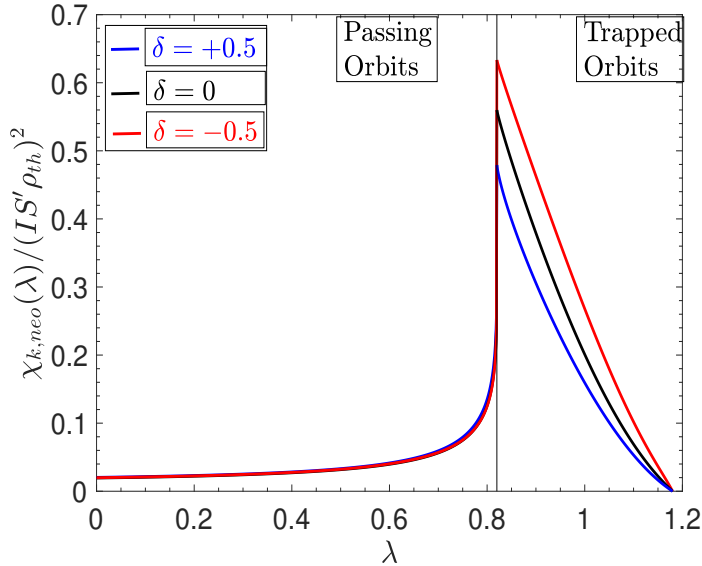
Figure 5. Pitch angle λ spectra of neoclassical dielectric susceptibility. Vertical back solid line marks the trapped-passing boundary. Parameters: $\frac{\partial R_0}{\partial r} = -0.4$, $S_\delta = 0.4$, $\kappa = 1.5$, $S_\kappa = 1$, $\epsilon = 0.18$, $q = 3$.

3. Shaping effect on particle orbits: Bounce time, bounce angle and radial excursion

It is commonly believed that the neoclassical zonal flow screening is correlated with the width of the orbit of the trapped particle. The common notion is that the smaller the banana width, the smaller the neoclassical polarization (and hence stronger the zonal flow residual) is. So, here we calculate the width of the trapped and passing orbits along with the respective bounce times and bounce angles to see if there is any correlation between orbital properties (especially orbit width) and neoclassical screening. The bounce/circulation time is defined as

$$\tau_b = \oint \frac{B d\theta}{v_\| \vec{B} \cdot \vec{\nabla} \theta} = \frac{B_0}{v \frac{\partial \psi}{\partial r}} \oint \frac{\mathcal{J} d\theta}{h \xi}, \tag{22}$$

where $\oint \to \int_{-\pi}^{+\pi}$ for passing particles and $\oint \to 2 \int_{-\theta_b}^{+\theta_b}$ for the trapped particles. θ_b is bounce angle at which $v_\| = 0$. This is given by the solution of the nonlinear equation

$$\cos\left(\theta_b + x \sin \theta_b\right) = \frac{\lambda - 1}{\epsilon}. \tag{23}$$

Using equations(12) and (B.9), the bounce time / circulation time for passing particles can be obtained as:

$$\tau_b = \frac{2\pi q R_0}{v\sqrt{1-\lambda}} \frac{\sum_{i=0}^{\infty} \epsilon^i a_i(\lambda) F_i}{\sum_{i=0}^{\infty} (-1)^i \epsilon^i F_i}. \tag{24}$$

The departure of the particle from the flux surface ψ due to magnetic drift $\vec{v}_d$ is

$$\Delta\psi = \int \vec{v}_d \cdot \vec{\nabla}\psi \frac{B d\theta}{v_\| \vec{B} \cdot \vec{\nabla}\theta}. \tag{25}$$

Note that the magnetic drift velocity $\vec{v}_d$ is :

$$\vec{v}_d = \frac{1}{\Omega_{ci}} \frac{1}{2} \left(v_\perp^2 + 2v_\|^2\right) \frac{\vec{B} \times \vec{\nabla}B}{B^2}. \tag{26}$$

This yields for the radial component :

$$\vec{v}_d \cdot \vec{\nabla}\psi = \frac{v^2}{2\Omega_{ci}} \left(1 + \xi^2\right) \frac{I}{B^2 J} \frac{\partial B}{\partial \theta}. \tag{27}$$

Here $\xi^2 = v_\parallel^2/v^2 = 1 - \lambda/h$, λ is pitch angle and $h = R/R_0$. Then, the departure of the particle from the flux surface ψ due to the radial magnetic drift becomes

$$\Delta\psi = \int \vec{v}_d \cdot \vec{\nabla}\psi \frac{B d\theta}{v_\parallel \vec{B} \cdot \vec{\nabla}\theta} = \frac{mvI}{2eB_0} \int d\theta \frac{1 + \xi^2}{\xi} \frac{\partial h}{\partial \theta}. \tag{28}$$

Hence, using $\left|\vec{\nabla}\psi\right|(\theta = 0) = R_0(1 + \epsilon)B_{p0}$, the radial excursion at the mid plane($\theta = 0$) becomes

$$\Delta r = \frac{\Delta\psi}{\left|\vec{\nabla}\psi\right|(\theta = 0)} = \frac{\rho_\theta}{2(1 + \epsilon)} \int d\theta \frac{1 + \xi^2}{\xi} \frac{\partial h}{\partial \theta}. \tag{29}$$

For passing particle the integral in the above equation is $\int \to \int_0^\pi$. For the trapped particle $\int \to 2\int_0^{\theta_b}$.

The bounce times and radial excursions of passing particles in pitch angle (λ) and triangularity (δ) space are shown in figure(6). It can be clearly seen that both the bounce time and radial excursion are *not* symmetric with respect to $\delta \to -\delta$. The degree of asymmetry ($|\tau_b(\delta^+) - \tau_b(\delta^-)|$) in the bounce time is strongest for pitch angles close to the trapped-passing boundary. Specifically, bounce time for negative triangularity is smaller than that for the positive triangularity i.e., $\tau_b(\delta^-) < \tau_b(\delta^+)$. The bounce time of passing particle monotonically increases with the pitch angle and diverges near the trapped-passing boundary. The radial excursion of passing particle shows non-monotonic variation in pitch angle, with a clear peak. The peak moves from low λ at high positive δ to high λ at high negative δ. The radial excursion monotonically decreases with decreasing δ at low pitch angles, such that that $\Delta r(\delta^-) < \Delta r(\delta^+)$. At high pitch angles, the radial excursion increases with decreasing δ such that $\Delta r(\delta^-) > \Delta r(\delta^+)$.
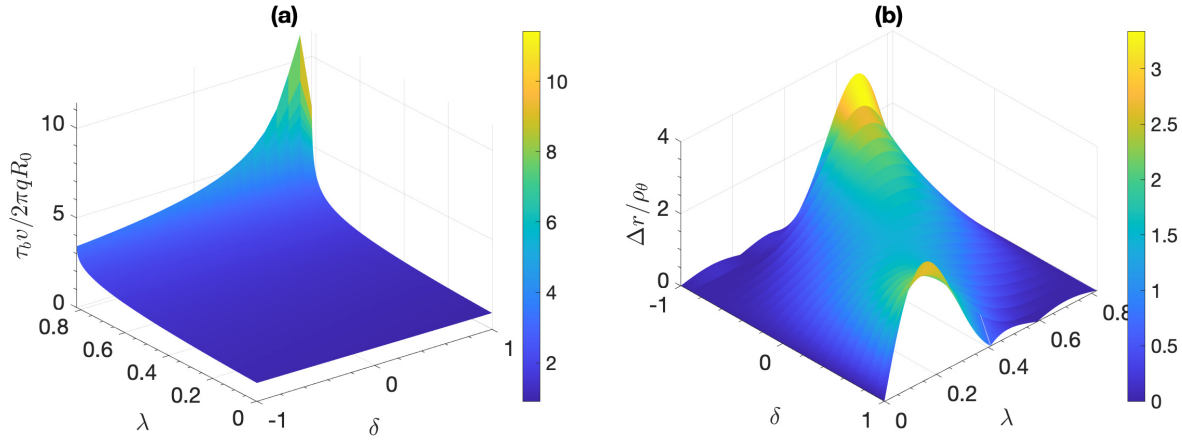
Figure 6. Bounce time τ_b (a) and radial excursion Δr (b) of passing particle as a function of pitch λ angle and triangularity δ. Bounce time for negative triangularity is lower than that for positive triangularity. Radial excursion decreases or increases with triangularity depending on the pitch angle.

Figure(7)(a) compares the bounce times of passing and trapped orbits at different positive and negative triangularities. While passing orbits exhibit significant dispersion with respect to δ near the trapped-passing boundary, trapped orbits show strong dispersion with respect to δ through out the trapping domain $\lambda = [1-\epsilon]$ to $\lambda = [1+\epsilon]$. Notice the opposite trend of bounce time in δ of the trapped orbits compared to that of passing orbits. That is $\tau_b(\delta^-) > \tau_b(\delta^+)$ for the trapped particles. Figure(7)(b) shows how the bounce angle is affected when changing the triangularity. It can be clearly seen that the bounce angle increases with decreasing triangularity, such that $\theta_b(\delta^-) > \theta_b(\delta^+)$. This means that the fraction of trapped particles spending time on the good curvature side increases with decreasing δ. The pitch angle spectra of the radial excursion of trapped particle shows that the radial excursion decreases with increasing pitch angle. This is shown in figure(8). The radial excursion of trapped particles is not symmetric with respect to $\delta \to -\delta$. Figure(8) shows that the radial excursion of trapped particle decreases with decreasing δ such that $\Delta r(\delta^-) < \Delta r(\delta^+)$. Cartoons of typical trapped orbits in negative, zero and positive triangularities, for a fixed pitch angle, are shown in figure(10). Notice that, *somewhat surprisingly, the banana widths are smaller, yet the neoclassical susceptibility is bigger in negative δ.* Trapping fraction $f_t = 1 - \frac{1}{2}\int_0^{1-\epsilon} d\lambda \frac{\int d\theta \mathcal{J}/h\xi}{\int d\theta \mathcal{J}}$ is calculated as a function of δ. Figure(9) shows that *the trapping fraction f_t increases with decreasing δ such that $f_t(\delta^-) > f_t(\delta^+)$.* These results are summarized in the table(**1**).

This resolves the somewhat counter-intuitive trend in the neoclassical susceptibility dependence on banana width.
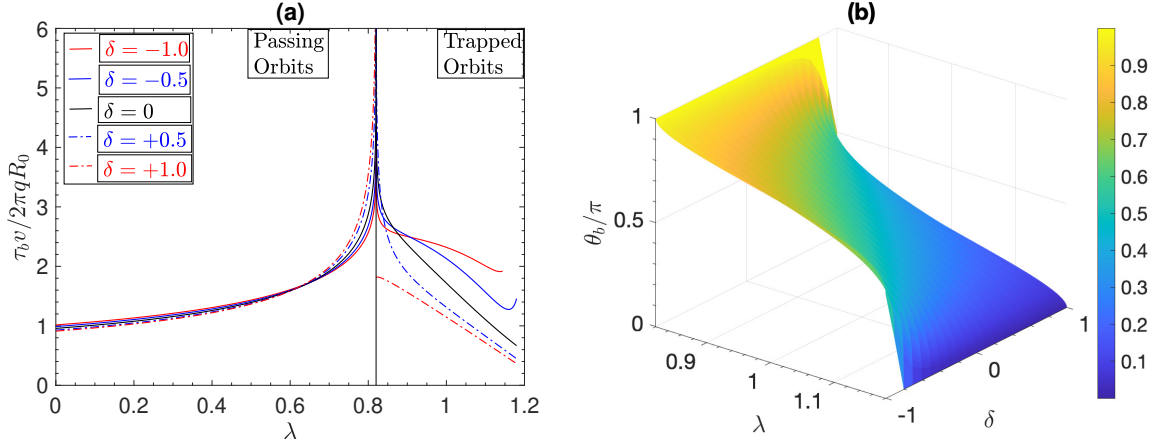

Figure 7. (a): Bounce time τ_b as a function of pitch angle λ with triangularity δ as a parameter. Vertical back solid line marks the trapped-passing boundary. (b): Bounce angle θ_b as a function of pitch angle λ and triangularity δ. θ_b is higher for negative δ than for positive δ.
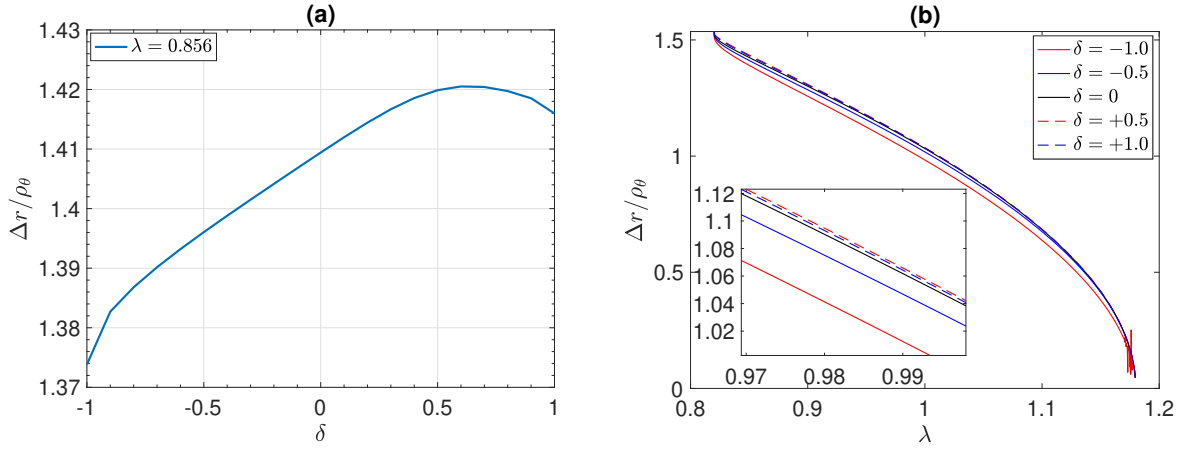
Figure 8. (a): Radial excursion (Δr) of trapped particle vs triangularity (δ). Radial excursion is smaller for negative triangularity than that for positive triangularity. (b): Radial excursion (Δr) of a trapped particle as a function of pitch angle (λ) at different triangularities (δ). The figure inset show a zoom in of a portion of the plot. The radial excursion decreases with increasing λ and decreasing δ.
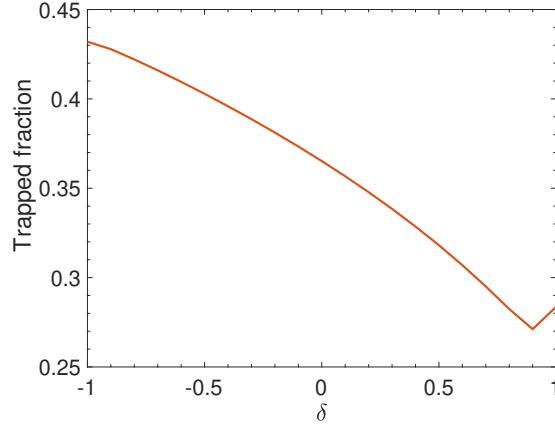
Figure 9. Fraction of trapped particles f_t increases on decreasing δ such that $f_t(\delta^-) > f_t(\delta^+)$.
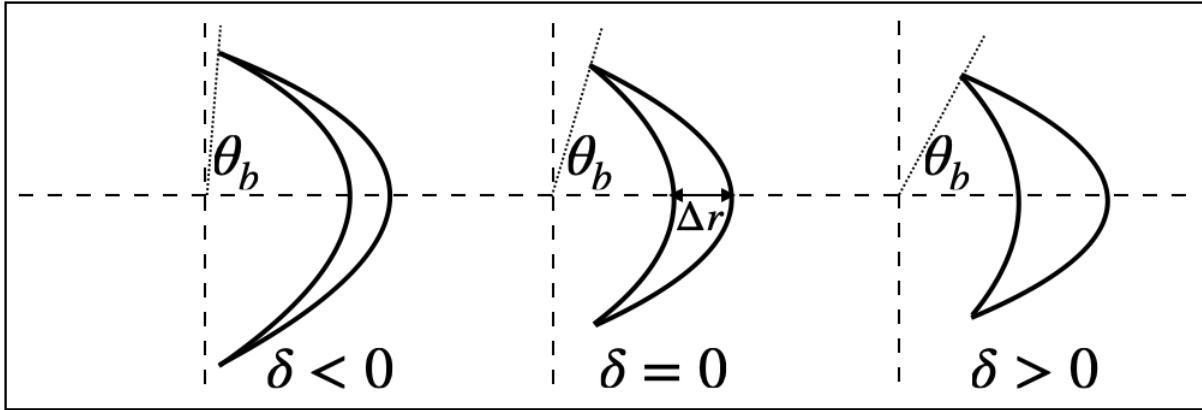
Figure 10. Cartoon of trapped orbits in negative, zero and positive triangularity for a fixed pitch angle.

	passing	trapped
Bounce time	$\tau_b^{\delta^-} < \tau_b^{\delta^+}$	$\tau_b^{\delta^-} > \tau_b^{\delta^+}$
Bounce angle		$\theta_b^{\delta^-} > \theta_b^{\delta^+}$
Radial excursion	$[\Delta r]^{\delta^-} < [\Delta r]^{\delta^+}$ for small λ, $[\Delta r]^{\delta^-} > [\Delta r]^{\delta^+}$ for large λ	$[\Delta r]^{\delta^-} < [\Delta r]^{\delta^+}$
Fractions	$f_p(\delta^-) < f_p(\delta^+)$	$f_t(\delta^-) > f_t(\delta^+)$

Table 1. Summary of results on triangularity effect on particle orbits.

This analysis questions the often-made claim that smaller banana width always

corresponds to smaller neoclassical polarization. A decrease in radial excursion does not always correspond to a decrease in neoclassical polarization. However, notice that the trend of bounce angle in δ and λ correlates well with the trend of neoclassical susceptibility/ polarization in δ and λ (in the trapped part of the λ-spectrum). Also, an increase in trapping fraction correlates well with increase in neoclassical susceptibility. This means that the decrease in neoclassical susceptibility due to the lower excursion radius is offset by the increase in neoclassical susceptibility due to the increase in trapped fraction. This is not surprising, given the fact that the neoclassical polarization density is the difference between the trapped/passing density and the bounce/transit gyro-center density. The dominant contribution to the total neoclassical polarization density comes from the difference of trapped particle density and the bounce gyro-center density. With increasing trapped fraction the neoclassical polarization density increases! This means that the neoclassical susceptibility *increases* with the increasing trapped fraction.

4. Discussions and Conclusions

Zonal flows are well known to reduce turbulent transport and improve confinement [24]. Observation of improved confinement in negative triangularity L mode discharges has motivated this research to re-evaluate the role of zonal flows, if any, in improving confinement in negative triangularity shapes. The zonal flow shear is (in part) controlled by the zonal flow screening length, which is primarily determined by the neoclassical dielectric susceptibility [25]. Neoclassical dielectric susceptibility also sets the level of zonal flow residual [20, 26]. Reduction in banana width is often associated with reduction in neoclassical polarization. So, here we studied flux surface shaping effects on susceptibility, zonal flow screening length and particle orbits with a focus on effects manifested by varying triangularity. The main results are:

(i) Both classical dielectric susceptibility ($\chi_{k,cl}$) and neoclassical dielectric suscepti-bility ($\chi_{k,neo}$) *increase* with decreasing triangularity (δ), such that both suscep-tibilities are higher for negative triangularity than for positive triangularity i.e., $\chi_{k,cl}(\delta^-) > \chi_{k,cl}(\delta^+)$ and $\chi_{k,neo}(\delta^-) > \chi_{k,neo}(\delta^+)$. Neoclassical susceptibility is al-ways greater than the classical susceptibility i.e., $\chi_{k,neo} \gg \chi_{k,cl}$. As a result, the zonal flow residual is *lower* for negative triangularity than that for positive trian-gularity. The zonal flow screening length l_z, given by $l_z = \sqrt{\chi_{tot}/k_r^2}$, is *larger* in negative triangularity than for positive triangularity i.e., $l_z(\delta^-) > l_z(\delta^+)$. Gyroki-netic simulations support the analytic predictions. The zonal flow residual calcu-lated using GENE simulations follows a trend in δ similar to that of the analytic predictions.

(ii) The pitch angle spectra of neoclassical susceptibility $\chi_{k,neo}$ peaks at the trapped-passing boundary. The dominant contribution to $\chi_{k,neo}$ is from trapped orbits. The trapped part of the spectrum is *elevated* when $\delta \to -\delta$. The passing part of the spectrum is weakly affected by δ.

(iii) Particle orbit calculations show that *the banana width is reduced in negative triangularity as compared to positive triangularity.* Yet, surprisingly the neoclassical dielectric susceptibility is *higher* in negative triangularity! This is because of the increase in trapped fraction and the bounce angles for negative triangularity, as compared to those for positive triangularity. In fact, *the polarization reduction by banana width reduction is offset by polarization enhancement due to an increase in trapped fraction.*

These results can be concisely and clearly summarized through the flowchart shown in figure(11).
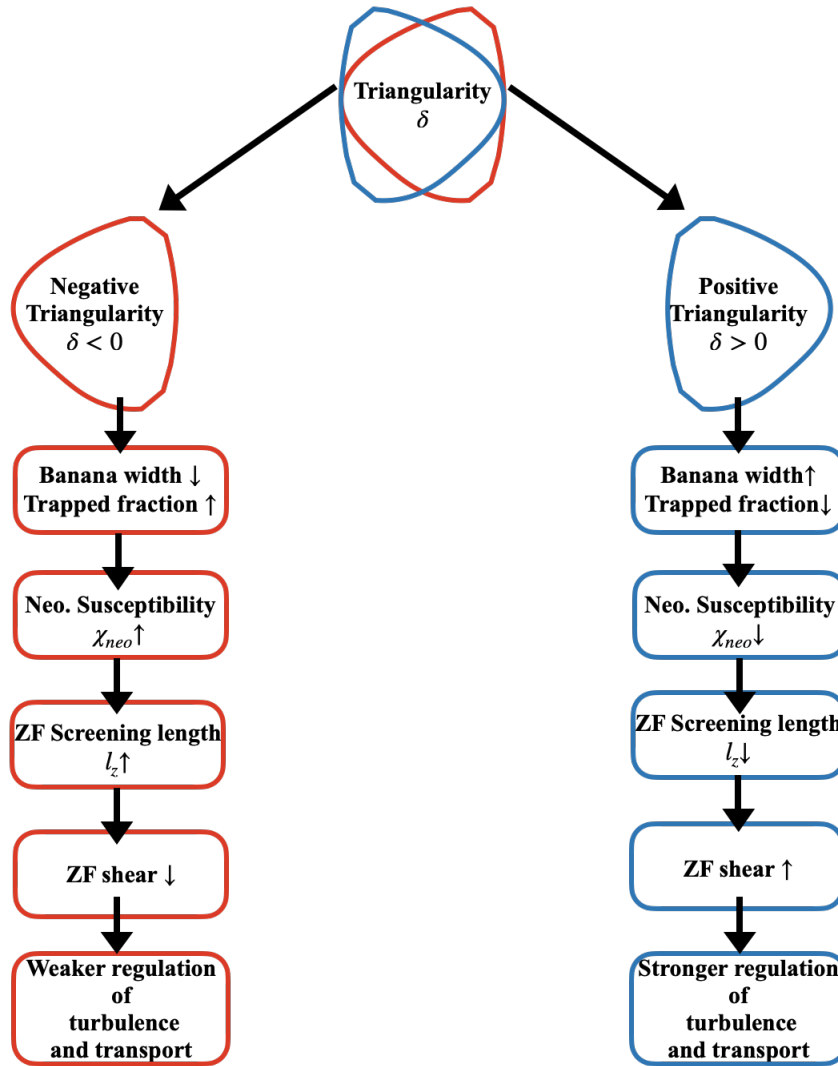
Figure 11. Flow chart of results discussed in text. Upward pointing arrow ↑ means "larger" and downward pointing arrow ↓ means "smaller".

A bigger screening length implies a weaker zonal flow shear for fixed drive. This suggests weaker feedback effects i.e., weaker regulation of turbulence and transport by zonal flows. Thus, core transport improvement in negative triangularity cannot be attributed to simple elements of zonal flow physics. Then, *what is the reason for improved confinement in negative triangularity?* While linear stabilization of the TEM mode is invoked to explain this [4,12], more detailed study of flux surface shaping effect on nonlinear saturation mechanism is desirable. Our results here are consistent with the findings of Ref [27]. That study showed, via nonlinear GENE simulations for ITG

turbulence, that zonal flows have a weaker effect on turbulence regulation in negative triangularity than in positive triangularity. This was demonstrated by analyzing the effect of removing the zonal component in both positive and negative triangularities. That study did not, however, offer a physics understanding as to why zonal flow effects are weaker in negative triangularity.

It is now known that zonal flows play a role in the L-H transition [28–33]. The L-H power threshold is much higher in negative triangularity than that in positive triangularity. This disparity is of crucial importance and its understanding is the key physics issue for understanding confinement in negative triangularity. Noting the result obtained here -i.e., that zonal flows are weaker for negative triangularity than for positive triangularity, -one might be tempted to link the increased L-H threshold to weaker zonal shear in negative triangularity. In fact, a causal relationship along this line is possible, but has not been established. However, one should also note that negative triangularity degrades the stability of edge plasma to high-n ballooning modes, so that access to second stability is blocked in negative triangularity [34]. The pedestal pressure gradient fails to exceed the ballooning stability limit. This prevents diamagnetic rotation shear - driven feedback on turbulence, which promotes transport suppression and 'locks in' the H-mode. Thus, the negative triangularity edge is expected to remain in L mode even at high heating power. Further studies are required to sort out which effect is the more important one.

Additionally, we add that the screening length, residual etc., are only one aspect of zonal flow physics. In steady state, zonal flow energy level is set by the balance of Reynolds power and the collisional dissipation. The Reynolds stress depends on the state of turbulence and the temperature, density gradients, and the geometry of magnetic flux surfaces. Turbulence level and the equilibrium gradients are also affected by the

magnetic geometry. Thus Reynolds stress/ power (and hence the zonal flow energy) has a complicated dependence on the magnetic geometry. The simple argument here is that a bigger screening length implies a weaker zonal flow for fixed drive.

Energetic particles and impurities affect the residual level of zonal flow. But this effect is not significant in the long wave length regime $k_r \rho_\theta \ll 1$, which is the regime of calculations in this paper. This does *not* mean that there is no effect of energetic particles on zonal flows. In fact, in the shorter wave length regime $k_r \rho_i < 1 < k_r \rho_\alpha$ (ρ_α is energetic ion gyro-radius), the residual level of zonal flow is enhance by energetic particles, due to enhanced classical polarization and reduced neoclassical polarization by energetic particles [35]. This is possibly a reason of micro-turbulence reduction by energetic particles with moderate energies when TAEs are not excited. Recently, MeV range energetic ions driven TAEs has been shown to excite stronger large scale zonal flows [36]. This in turn further suppresses the turbulence and transport driven by ITG/TEM. This is beneficial for plasma operation in the reactor regime. Then, the important question here is what is the fate of the zonal flows driven by energetic particles induced TAEs in negative triangularity reactor scenario? This will be studied in future.

Impurities also exhibit a trend similar to that of energetic particles for the zonal flow residual in the intermediate wave length regime [37]. The question of how this is affected by positive and negative triangularity is interesting and has implications for transport and confinement in burning plasma reactor conditions. One expects the corresponding residuals to be lower for negative triangularity than for positive triangularity. However, exact calculations are needed for an accurate quantitative prediction. This is beyond the scope of this paper and is left as a future work.

Can the predictions here on zonal flow screening length vs triangularity be tested

experimentally? This is difficult to answer. Note, however, that the zonal flow radial correlation length should show a 'footprint' of zonal flow screening. We propose that the radial correlation length of the zonal flow can be used as a proxy for the zonal flow screening length. BES velocimetry [38] can be exploited to extract the radial correlation length of zonal flow from direct measurements of zonal velocity correlations $\langle v_{zf}(r_1) v_{zf}(r_2) \rangle$. Thus, one can compare the zonal flow radial correlation lengths for positive and negative triangularity, under otherwise similar conditions. This is a potentially interesting experiment, which should be pursued.

Acknowledgments

Appendix A. Calculation of classical susceptibility $\chi_{k,cl}$

Recall that $\vec{k}_r = \vec{\nabla}S = S'\vec{\nabla}\psi = S'\partial_r\psi\vec{\nabla}r$ so that $k_r^2 = S'^2\left(\partial_r\psi\right)^2\frac{R^2}{\mathcal{J}^2}g_{\theta\theta} = S'^2 B_p^2 R^2$ and hence the classical polarization is proportional to

$$\left\langle k_r^2/B^2 \right\rangle = S'^2 \left\langle B_p^2 R^2/B^2 \right\rangle = S'^2 \left(\partial_r\psi\right)^2 \frac{\oint d\theta \frac{R^2}{\mathcal{J}B^2}g_{\theta\theta}}{\oint d\theta \mathcal{J}} \tag{A.1}$$

The integral in the denominator is of the equation(A.1) can be evaluated as

$$\oint d\theta \mathcal{J} = \kappa r R_0 \oint d\theta h\left[R_0'\cos(\theta) + \cos\left(x\sin\theta\right) + \sin(y)\sin\theta\left\{S_\kappa - S_\delta\cos\theta + (1+S_\kappa)x\cos\theta\right\}\right]$$

$$= \kappa r R_0\left[F_0 + \epsilon F_1\right] \tag{A.2}$$

The integral in the numerator of equation(A.1) is

$$\oint d\theta \frac{R^2}{\mathcal{J}B^2} g_{\theta\theta} \approx \frac{r^2}{\epsilon\kappa B_0^2} \oint d\theta \frac{[1 + \epsilon\cos y]^3 \left\{\sin^2 y \left[1 + x\cos\theta\right]^2 + \kappa^2\cos^2\theta\right\}}{[R_0'\cos(\theta) + \cos(x\sin\theta) + \sin(y)\sin\theta\left\{S_\kappa + ((1 + S_\kappa)x - S_\delta)\cos\theta\right\}]}$$

$$= \frac{r^2}{\epsilon\kappa B_0^2} f \quad (say) \tag{A.3}$$

Using equations(A.1),(A.2) and (A.3), it is straight forward to get the expression for

the classical susceptibility given by equation(15).

Appendix B. Calculation of Neo-classical susceptibility $\chi_{k,neo}$

The integral $\left\langle \int d^3v F_M \left(\frac{v_\parallel}{B}\right)^2 \right\rangle$ appearing in equation(3) is calculated first. This can be

calculated exactly.

$$\left\langle \int d^3v F_M \left(\frac{v_\parallel}{B}\right)^2 \right\rangle = \frac{n_0 T}{m_i} \left\langle \frac{1}{B^2} \right\rangle = \frac{n_0 T}{m_i B_0^2} \frac{\oint d\theta \mathcal{J} h^2}{\oint d\theta \mathcal{J}} \tag{B.1}$$

$$= \frac{n_0 T}{m_i B_0^2} \frac{F_0 + 3\epsilon F_1 + 3\epsilon^2 F_2 + \epsilon^3 F_3}{F_0 + \epsilon F_1} \tag{B.2}$$

Calculation of $\left\langle \int d^3v F_M \frac{v_\parallel}{B} \overline{\left(\frac{v_\parallel}{B}\right)} \right\rangle$ follows next. It is easy to show that

$$\left\langle \int d^3v F_M \frac{v_\parallel}{B} \overline{\left(\frac{v_\parallel}{B}\right)} \right\rangle = \left\langle \int d^3v F_M \overline{\left(\frac{v_\parallel}{B}\right)}^2 \right\rangle \tag{B.3}$$

Now it is useful to transform the volume element from the velocity space to energy (E)

- pitch angle (λ) space.

$$d^3v = \sum_\sigma \frac{\pi v^3}{|v_\parallel|} \frac{B}{B_0} dv d\lambda = \frac{4\pi E dE d\lambda}{m^2 |v_\parallel| h} = \frac{4\pi E dE d\lambda}{m^2 v |\xi| h}, \tag{B.4}$$

where we have used $E = mv^2/2 + Ze\phi$ and $v_\parallel = v(1 - \lambda B/B_0)^{1/2} \implies \xi = (1 - \lambda/h)^{1/2}$.

Here λ is pitch angle. Hence,

$$
\left\langle \int d^3v F_M \frac{v_\parallel}{B} \overline{\left(\frac{v_\parallel}{B}\right)} \right\rangle = \frac{1}{\oint d\theta \mathcal{J}} \oint d\theta \mathcal{J} \int dE d\lambda \frac{4\pi E}{m^2 |v_\parallel| h} F_M \overline{\left(\frac{v_\parallel}{B}\right)}^2
$$

$$
= \frac{1}{\oint d\theta \mathcal{J}} \oint d\theta \mathcal{J} \int dE d\lambda \frac{4\pi E}{m^2 |v_\parallel| h} F_M \left[\frac{\int d\theta \frac{\mathcal{J}B}{v_\parallel} \left(\frac{v_\parallel}{B}\right)}{\int d\theta \frac{\mathcal{J}B}{v_\parallel}} \right]^2
$$

$$
= \frac{4\pi}{m^2 B_0^2} \sqrt{\frac{2}{m}} \left(\int dE E^{3/2} F_M \right) \left(\oint d\theta \mathcal{J} \right) \int d\lambda \frac{1}{\int d\theta \frac{\mathcal{J}}{h\xi}}
$$

$$
= \frac{3}{2} \frac{n_0 T}{m B_0^2} \left(\oint d\theta \mathcal{J} \right) \int_0^{1-\epsilon} d\lambda \frac{1}{\oint d\theta \frac{\mathcal{J}}{h\xi}}, \tag{B.5}
$$

where the last step makes use of the fact that $\int_0^\infty dE E^{3/2} F_M = 2n_0 T \left(\frac{m}{2\pi}\right)^{3/2} \frac{3\sqrt{\pi}}{8}$ and

only passing particle integral needs be considered. The denominator of equation(B.5) is

$$
\oint d\theta \frac{\mathcal{J}}{h\xi} = \frac{R_0 \kappa r}{\sqrt{1-\lambda}}
$$

$$
\times \oint d\theta \frac{h^{1/2} \left[R_0' \cos(\theta) + \cos(x \sin \theta) + \sin(y) \sin \theta \{ S_\kappa + ((1 + S_\kappa)x - S_\delta) \cos \theta \} \right]}{\left(1 + \frac{\epsilon}{1-\lambda} \cos y \right)^{1/2}}
$$

$$
\tag{B.6}
$$

Taylor expanding for small inverse aspect ratio yields

$$
\frac{(1 + \epsilon \cos y)^{1/2}}{\left(1 + \frac{\epsilon}{1-\lambda} \cos y \right)^{1/2}} = \sum_{i=0}^\infty \epsilon^i a_i(\lambda) \cos^i y, \tag{B.7}
$$

Pitch angle dependent first few coefficients $\{a_i(\lambda)\}$ in equation(B.7) are obtained as

$$
\begin{cases}
a_0(\lambda) &= \quad 1 \\[2mm]
a_1(\lambda) &= \quad \frac{1}{2}\left(1 - \frac{1}{1-\lambda}\right) \\[2mm]
a_2(\lambda) &= \quad \frac{3}{8}\frac{1}{(1-\lambda)^2} - \frac{1}{4}\frac{1}{1-\lambda} - \frac{1}{8} \\[2mm]
a_3(\lambda) &= \quad -\frac{5}{16}\frac{1}{(1-\lambda)^3} + \frac{3}{16}\frac{1}{(1-\lambda)^2} + \frac{1}{16}\frac{1}{(1-\lambda)} + \frac{1}{16} \\[2mm]
\cdots \quad \cdots & \qquad\qquad \cdots
\end{cases} \tag{B.8}
$$

Hence, equation(B.6) becomes

$$\oint d\theta \frac{\mathcal{J}}{h\xi} = \frac{R_0 \kappa r}{\sqrt{1-\lambda}} \sum_{i=0}^{\infty} \epsilon^i a_i(\lambda) F_i, \tag{B.9}$$

which can be inverted to yield

$$\frac{1}{\oint d\theta \frac{\mathcal{J}}{h\xi}} = \frac{\sqrt{1-\lambda}}{R_0 \kappa r} \frac{1}{F_0} \left[1 - \sum_{i=1}^{\infty} \epsilon^i b_i(\lambda) \right], \tag{B.10}$$

where

$$\begin{cases} b_1 & = & a_1(\lambda) F_1/F_0 \\ b_2 & = & a_2(\lambda) F_2/F_0 \\ b_3 & = & a_3(\lambda) F_3/F_0 \\ \dots & \dots & \dots \end{cases} \tag{B.11}$$

Finally, using the following integrals

$$\int_0^{1-\epsilon} d\lambda \sqrt{1-\lambda} a_0(\lambda) = -\frac{2}{3} \left(\epsilon^{3/2} - 1 \right) \tag{B.12}$$

$$\int_0^{1-\epsilon} d\lambda \sqrt{1-\lambda} a_1(\lambda) = -\frac{1}{3}\epsilon^{3/2} + \epsilon^{1/2} - \frac{2}{3} \tag{B.13}$$

$$\int_0^{1-\epsilon} d\lambda \sqrt{1-\lambda} a_2(\lambda) = \frac{1}{12}\epsilon^{3/2} + \frac{1}{2}\epsilon^{1/2} - \frac{4}{3} + \frac{3}{4}\epsilon^{-1/2} \tag{B.14}$$

$$\int_0^{1-\epsilon} d\lambda \sqrt{1-\lambda} a_3(\lambda) = -\frac{1}{24}\epsilon^{3/2} - \frac{1}{8}\epsilon^{1/2} + \frac{3}{8}\epsilon^{-1/2} - \frac{5}{24}\epsilon^{-3/2} \tag{B.15}$$
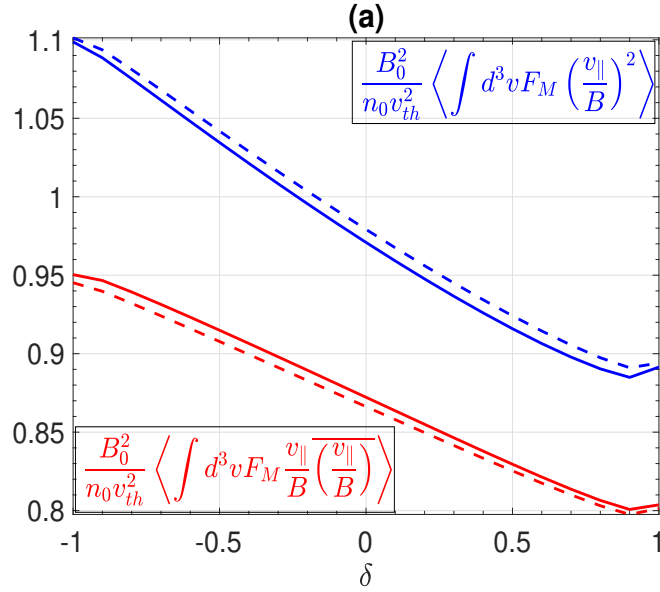
the equation(B.5), for the small inverse aspect ratio ($\epsilon \ll 1$), reduces to

$$\left\langle \int d^3 v F_M \frac{v_\parallel}{B} \overline{\left(\frac{v_\parallel}{B} \right)} \right\rangle = \frac{n_0 T}{m B_0^2} \left(1 + \epsilon \frac{F_1}{F_0} \right) \left[1 + \epsilon \frac{F_1}{F_0} + \sum_{i=1}^{\infty} \epsilon^{1+i/2} A_{1+i/2} \right], \tag{B.16}$$

where the first few terms $\{A_{1+i/2}\}$ are

$$
\left\{
\begin{array}{rcc}
A_{3/2} & = & -1 - \frac{3}{2}\frac{F_1}{F_0} - \frac{9}{8}\frac{F_2}{F_0} + \frac{5}{16}\frac{F_3}{F_0} \\[2mm]
A_2 & = & 2\frac{F_2}{F_0} \\[2mm]
A_{5/2} & = & \frac{1}{2}\frac{F_1}{F_0} - \frac{3}{4}\frac{F_2}{F_0} - \frac{9}{16}\frac{F_3}{F_0} \\[2mm]
A_3 & = & 0 \\[2mm]
A_{7/2} & = & -\frac{1}{8}\frac{F_2}{F_0} + \frac{3}{16}\frac{F_3}{F_0} \\[2mm]
\cdots & \cdots & \cdots
\end{array}
\right\}
\tag{B.17}
$$

The variations of the integrals $\left\langle \int d^3 v F_M \left(\frac{v_\parallel}{B}\right)^2 \right\rangle$ and $\left\langle \int d^3 v F_M \frac{v_\parallel}{B} \overline{\left(\frac{v_\parallel}{B}\right)} \right\rangle$ with triangularity are shown in figure(B1). The figure shows that both integrals increase with decreasing triangularity such that the respective values are higher in negative triangularity, as compared to positive triangularity. Also notice that the difference of the integrals are bigger for negative triangularity than for positive triangularity. The difference of the integrals times $\frac{m_i I S'}{e}$ yields the expression for neoclassical susceptibility given by equation(17).

Figure B1. (a): Difference of blue and red curves give a measure of neoclassical susceptibility. The blue dashed curve correspond to the small inverse aspect ratio analytic approximation equation(B.2). The red dashed curve correspond to the small inverse aspect ratio analytic approximation equation(B.16). Solid curve correspond to the result obtained using the numerical integration of equations(B.1) and (B.5). Parameters: $\frac{\partial R_0}{\partial r} = -0.4$, $S_\delta = 0.4$, $\kappa = 1.5$, $S_\kappa = 1$, $\epsilon = 0.18$, $q = 3$.

Appendix C. Variation of zonal flow residual with elongation κ

Variation of the residual zonal flow with elongation κ, obtained from the analytic equation(20), is shown in the figure(C1). It shows that the residual level increases with the elongation. This trend is similar to that obtained in Ref [39]. The increasing trend of the residual with κ is because of the increasing trend of the classical susceptibility $\chi_{k,cl}$ with κ. This is shown in the bottom panel of figure(C1), which is plotted using equation(15). Note, from equations(17) and (14), that the neoclassical susceptibility $\chi_{k,neo}$ is independent of κ. As a result the ratio $\chi_{k,neo}/\chi_{k,cl}$ decreases and hence the zonal flow residual increases with κ.
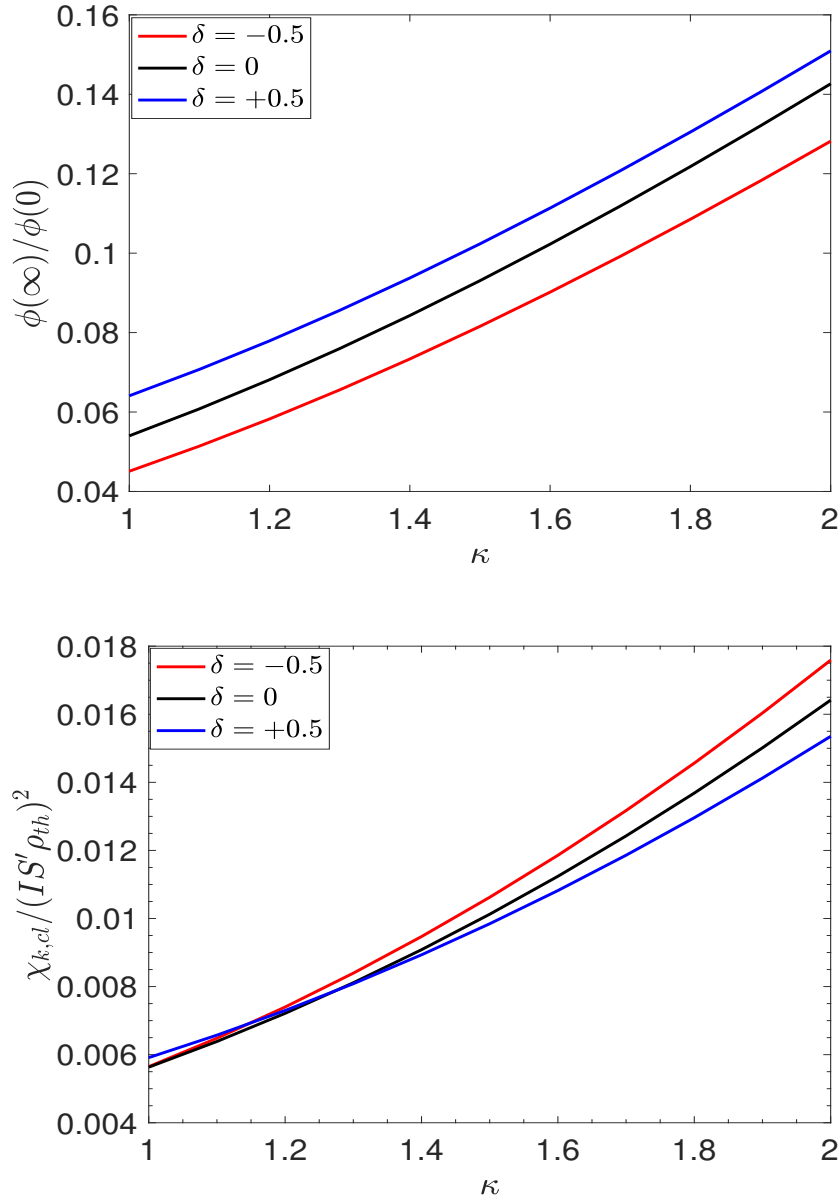
Figure C1. Top: Variation of residual zonal flow level with elongation κ at different triangularities δ. Parameters: $\frac{\partial R_0}{\partial r} = -0.4$, $S_\delta = 0.4$, $S_\kappa = 1$, $\epsilon = 0.18$, $q = 3$. Residual level increases with κ. Bottom: Classical susceptibility $\chi_{k,cl}$ increases with elongation κ.

[1] Austin M E, Marinoni A, Walker M L, Brookman M W, deGrassie J S, Hyatt A W, McKee G R, Petty C C, Rhodes T L, Smith S P, Sung C, Thome K E and Turnbull A D 2019 *Phys. Rev. Lett.* **122**(11) 115001 URL `https://link.aps.org/doi/10.1103/PhysRevLett.122.115001`

[2] Marinoni A, Austin M E, Hyatt A W, Walker M L, Candy J, Chrystal C, Lasnier C J, McKee G R, OdstrÄil T, Petty C C, Porkolab M, Rost J C, Sauter O, Smith S P, Staebler G M, Sung C, Thome K E, Turnbull A D and Zeng L 2019 *Physics of Plasmas* **26** 042515 (*Preprint*

https://doi.org/10.1063/1.5091802) URL https://doi.org/10.1063/1.5091802

[3] Fontana M, Porte L, Coda S and and O S 2017 *Nuclear Fusion* **58** 024002 URL https://doi.org/10.1088/1741-4326/aa98f4

[4] Camenen Y, Pochelon A, Behn R, Bottino A, Bortolon A, Coda S, Karpushov A, Sauter O, Zhuang G and the TCV team 2007 *Nuclear Fusion* **47** 510–516 URL https://doi.org/10.1088/0029-5515/47/7/002

[5] Coda S, Merle A, Sauter O, Porte L, Bagnato F, Boedo J, Bolzonella T, Février O, Labit B, Marinoni A, Pau A, Pigatto L, Sheikh U, Tsui C, Vallar M and Vu T 2021 *Plasma Physics and Controlled Fusion* **64** 014004 URL https://doi.org/10.1088/1361-6587/ac3fec

[6] Wagner F, Becker G, Behringer K, Campbell D, Eberhagen A, Engelhardt W, Fussmann G, Gehre O, Gernhardt J, Gierke G v, Haas G, Huang M, Karger F, Keilhacker M, Klüber O, Kornherr M, Lackner K, Lisitano G, Lister G G, Mayer H M, Meisel D, Müller E R, Murmann H, Niedermeyer H, Poschenrieder W, Rapp H, Röhr H, Schneider F, Siller G, Speth E, Stäbler A, Steuer K H, Venus G, Vollmer O and Yü Z 1982 *Phys. Rev. Lett.* **49**(19) 1408–1412 URL https://link.aps.org/doi/10.1103/PhysRevLett.49.1408

[7] Wagner F 2007 *Plasma Physics and Controlled Fusion* **49** B1–B33 URL https://doi.org/10.1088/0741-3335/49/12b/s01

[8] Evans T E, Moyer R A, Thomas P R, Watkins J G, Osborne T H, Boedo J A, Doyle E J, Fenstermacher M E, Finken K H, Groebner R J, Groth M, Harris J H, La Haye R J, Lasnier C J, Masuzaki S, Ohyabu N, Pretty D G, Rhodes T L, Reimerdes H, Rudakov D L, Schaffer M J, Wang G and Zeng L 2004 *Phys. Rev. Lett.* **92**(23) 235003 URL https://link.aps.org/doi/10.1103/PhysRevLett.92.235003

[9] Han W, Offeddu N, Golfinopoulos T, Theiler C, Tsui C, Boedo J, Marmar E and the TCV Team 2021 *Nuclear Fusion* **61** 034003 URL https://doi.org/10.1088/1741-4326/abdb95

[10] Kikuchi M, Takizuka T, Medvedev S, Ando T, Chen D, Li J, Austin M, Sauter O, Villard L, Merle A, Fontana M, Kishimoto Y and Imadera K 2019 *Nuclear Fusion* **59** 056017 URL https://doi.org/10.1088/1741-4326/ab076d

[11] Paz-Soldan C 2021 *Plasma Physics and Controlled Fusion* **63** 083001 URL https://doi.org/10.1088/1361-6587/ac048b

[12] Marinoni A, Brunner S, Camenen Y, Coda S, Graves J P, Lapillonne X, Pochelon A, Sauter O and Villard L 2009 *Plasma Physics and Controlled Fusion* **51** 055016 URL https://doi.org/

10.1088/0741-3335/51/5/055016

[13] Merlo G, Huang Z, Marini C, Brunner S, Coda S, Hatch D, Jarema D, Jenko F, Sauter O and Villard L 2021 *Plasma Physics and Controlled Fusion* **63** 044001 URL https://doi.org/10.1088/1361-6587/abe39d

[14] Fontana M, Porte L, Coda S, Sauter O, Brunner S, Jayalekshmi A C, Fasoli A and and G M 2019 *Nuclear Fusion* **60** 016006 URL https://doi.org/10.1088/1741-4326/ab4d75

[15] Merlo G, Fontana M, Coda S, Hatch D, Janhunen S, Porte L and Jenko F 2019 *Physics of Plasmas* **26** 102302 (*Preprint* https://doi.org/10.1063/1.5115390) URL https://doi.org/10.1063/1.5115390

[16] Diamond P H, S-I Itoh, Itoh K and Hahm T S 2005 *Plasma. Phys. Cont* **47** R35–R161

[17] Starr V P 1968 *Physics of negative viscosity phenomena* (McGraw-Hill)

[18] Singh R and Diamond P H 2021 *Plasma Physics and Controlled Fusion* **63** 035015 URL https://doi.org/10.1088/1361-6587/abd618

[19] Biglari H, Diamond P H and Terry P W 1990 *Physics of Fluids B: Plasma Physics* **2** 1–4 (*Preprint* https://doi.org/10.1063/1.859529) URL https://doi.org/10.1063/1.859529

[20] Hinton F L and Rosenbluth M N 1999 *Plasma Physics and Controlled Fusion* **41** A653 URL http://stacks.iop.org/0741-3335/41/i=3A/a=059

[21] Miller R L, Chu M S, Greene J M, Lin-Liu Y R and Waltz R E 1998 *Physics of Plasmas* **5** 973–978 (*Preprint* https://doi.org/10.1063/1.872666) URL https://doi.org/10.1063/1.872666

[22] URL https://genecode.org/

[23] Jenko F 2000 *Computer Physics Communications* **125** 196–209 ISSN 0010-4655 URL https://www.sciencedirect.com/science/article/pii/S0010465599004890

[24] Lin Z, Hahm T S, Lee W W, Tang W M and White R B 1998 *Science* **281** 1835–1837 ISSN 0036-8075 (*Preprint* https://science.sciencemag.org/content/281/5384/1835.full.pdf) URL https://science.sciencemag.org/content/281/5384/1835

[25] Singh R and Diamond P 2021 *Nuclear Fusion* **61** 076009 URL https://doi.org/10.1088/1741-4326/abfadb

[26] Rosenbluth M N and Hinton F L 1998 *Phys. Rev. Lett.* **80** 724–727

[27] Duff J M, Faber B J, Hegna C C, Pueschel M J and Terry P W 2022 *Physics of Plasmas* **29** 012303 (*Preprint* https://doi.org/10.1063/5.0065585) URL https://doi.org/10.1063/5.0065585

[28] Kim E j and Diamond P H 2003 *Phys. Rev. Lett.* **90**(18) 185006 URL `https://link.aps.org/doi/10.1103/PhysRevLett.90.185006`

[29] Schmitz L, Zeng L, Rhodes T L, Hillesheim J C, Doyle E J, Groebner R J, Peebles W A, Burrell K H and Wang G 2012 *Phys. Rev. Lett.* **108**(15) 155002 URL `https://link.aps.org/doi/10.1103/PhysRevLett.108.155002`

[30] Conway G D, Angioni C, Ryter F, Sauter P and Vicente J (ASDEX Upgrade Team) 2011 *Phys. Rev. Lett.* **106**(6) 065001 URL `https://link.aps.org/doi/10.1103/PhysRevLett.106.065001`

[31] Tynan G, Xu M, Diamond P, Boedo J, Cziegler I, Fedorczak N, Manz P, Miki K, Thakur S, Schmitz L, Zeng L, Doyle E, McKee G, Yan Z, Xu G, Wan B, Wang H, Guo H, Dong J, Zhao K, Cheng J, Hong W and Yan L 2013 *Nuclear Fusion* **53** 073053 URL `https://doi.org/10.1088/0029-5515/53/7/073053`

[32] Manz P, Xu G S, Wan B N, Wang H Q, Guo H Y, Cziegler I, Fedorczak N, Holland C, Muller S H, Thakur S C, Xu M, Miki K, Diamond P H and Tynan G R 2012 *Physics of Plasmas* **19** 072311 (*Preprint* `https://doi.org/10.1063/1.4737612`) URL `https://doi.org/10.1063/1.4737612`

[33] Xu G S, Wan B N, Wang H Q, Guo H Y, Zhao H L, Liu A D, Naulin V, Diamond P H, Tynan G R, Xu M, Chen R, Jiang M, Liu P, Yan N, Zhang W, Wang L, Liu S C and Ding S Y 2011 *Phys. Rev. Lett.* **107**(12) 125001 URL `https://link.aps.org/doi/10.1103/PhysRevLett.107.125001`

[34] Saarelma S, Austin M E, Knolker M, Marinoni A, Paz-Soldan C, Schmitz L and Snyder P B 2021 *Plasma Physics and Controlled Fusion* **63** 105006 URL `https://doi.org/10.1088/1361-6587/ac1ea4`

[35] Cho Y and Hahm T 2019 *Nuclear Fusion* **59** 066026 URL `https://doi.org/10.1088/1741-4326/ab0ed6`

[36] Mazzi S, Garcia J, Zarzoso D, Kazakov Y O, Ongena J, Dreval M, Nocente M, Stancar Z, Szepesi G, Eriksson J, Sahlberg A, Benkadda S and Contributors J 2022 *Nature Physics* **18** 776–782 URL `https://doi.org/10.1038/s41567-022-01626-8`

[37] Guo W, Wang L and Zhuang G 2017 *Nuclear Fusion* **57** 056012 URL `https://doi.org/10.1088/1741-4326/aa6415`

[38] McKee G R, Fonck R J, Jakubowski M, Burrell K H, Hallatschek K, Moyer R A, Rudakov D L, Nevins W, Porter G D, Schoch P and Xu X 2003 *Physics of Plasmas* **10** 1712–1719 URL `http://scitation.aip.org/content/aip/journal/pop/10/5/10.1063/1.1559974`

[39] Xiao Y and Catto P J 2006 *Physics of Plasmas* **13** 082307 (*Preprint* https://doi.org/10.1063/1.2266892) URL https://doi.org/10.1063/1.2266892